OUKA

**The University of Osaka
Institutional Knowledge Archive**

Title	High-throughput line-illumination Raman microscopy with multislit detection
Author(s)	Mochizuki, Kentaro; Kumamoto, Yasuaki; Maeda, Shunsuke et al.
Citation	Biomedical Optics Express. 2023, 14(3), p. 1015-1026
Version Type	VoR
URL	https://hdl.handle.net/11094/103326
rights	© 2023 Optica Publishing Group. Users may use, reuse, and build upon the article, or use the article for text or data mining, so long as such uses are for non-commercial purposes and appropriate attribution is maintained. All other rights are reserved.
Note	

High-throughput line-illumination Raman microscopy with multislit detection

KENTARO MOCHIZUKI,[1,2,10] YASUAKI KUMAMOTO,[1,3,10]
SHUNSUKE MAEDA,[1] MASATO TANUMA,[4] ATSUSHI KASAI,[4]
MASASHI TAKEMURA,[2] YOSHINORI HARADA,[2] HITOSHI
HASHIMOTO,[3,4,5,6,7] HIDEO TANAKA,[2] NICHOLAS ISAAC SMITH,[3,8]
AND KATSUMASA FUJITA[1,2,3,9,*]

[1]*Department of Applied Physics, Osaka University, Suita, Osaka 565-0871, Japan*
[2]*Department of Pathology and Cell Regulation, Kyoto Prefectural University of Medicine, Kamigyo-ku, Kyoto 602-8566, Japan*
[3]*Institute for Open and Transdisciplinary Research Initiatives, Osaka University, Suita, Osaka 565-0871, Japan*
[4]*Laboratory of Molecular Neuropharmacology, Graduate School of Pharmaceutical Sciences, Osaka University, Suita, Osaka 565-0871, Japan*
[5]*Molecular Research Center for Children's Mental Development, United Graduate School of Child Development, Osaka University, Kanazawa University, Hamamatsu University School of Medicine, Chiba University and University of Fukui, Suita, Osaka 565-0871, Japan*
[6]*Institute for Datability Science, Osaka University, Suita, Osaka 565-0871, Japan*
[7]*Department of Molecular Pharmaceutical Sciences, Graduate School of Medicine, Osaka University, Suita, Osaka 565-0871, Japan*
[8]*Biophotonics Laboratory, Immunology Frontier Research Center, Osaka University, Suita, Osaka 565-0871, Japan*
[9]*Advanced Photonics and Biosensing Open Innovation Laboratory, AIST-Osaka University, Osaka University, Suita, Osaka 565-0871, Japan*
[10]*These authors contributed equally*
[*]*fujita@ap.eng.osaka-u.ac.jp*

Abstract: Raman microscopy is an emerging tool for molecular imaging and analysis of living samples. Use of Raman microscopy in life sciences is, however, still limited because of its slow measurement speed for spectral imaging and analysis. We developed a multiline-illumination Raman microscope to achieve ultrafast Raman spectral imaging. A spectrophotometer equipped with a periodic array of confocal slits detects Raman spectra from a sample irradiated by multiple line illuminations. A comb-like Raman hyperspectral image is formed on a two-dimensional detector in the spectrophotometer, and a hyperspectral Raman image is acquired by scanning the sample with multiline illumination array. By irradiating a sample with 21 simultaneous illumination lines, we achieved high-throughput Raman hyperspectral imaging of mouse brain tissue, acquiring 1108800 spectra in 11.4 min. We also measured mouse kidney and liver tissue as well as conducted label-free live-cell molecular imaging. The ultrafast Raman hyperspectral imaging enabled by the presented technique will expand the possible applications of Raman microscopy in biological and medical fields.

1. Introduction

Raman microscopy is an emerging tool in life sciences for molecular imaging and analysis of living samples [1–4]. The technique enables label-free molecular imaging of cells and tissue using the "molecular fingerprint" provided by Raman spectroscopy. Since Raman microscopy does not require any pretreatment of samples such as fluorescent labeling, it is well-suited for biomedical applications such as intraoperative measurement in clinical medicine [5] and

quality control of transplanted cells in regenerative medicine [6]. Conventional laser-scanning Raman microscopy required a long exposure time for imaging a sample due to the intrinsic low Raman scattering efficiency. However, the development of fast Raman imaging techniques, *e.g.*, coherent anti-Stokes Raman scattering (CARS) microscopy [7–9], slit-scanning Raman microscopy [1,10], multifocus confocal Raman microscopy [11], stimulated Raman scattering (SRS) microscopy [12–14], surface-enhanced Raman scattering (SERS) microscopy [1,15,16], and compressed sensing in Raman microscopy [17,18] have expanded applications of Raman microscopy to live cell and tissue imaging. Those Raman imaging techniques can also be combined with super-resolution techniques [19–22] and Raman-tag techniques [23–27]. Hence, Raman microscopy applications have been expanding to a variety of target biological molecules and processes.

Use of Raman microscopy in life sciences is, nevertheless, limited and life scientists predominantly use confocal fluorescence microscopy, although the fluorescence measurement requires pretreatment of a sample with additional chemicals, and depending on the fluorescent dye, may be incompatible with live imaging. In spontaneous Raman microscopy, which provides the inherent molecular fingerprint of the sample without using a dye, a weak point is the far slower measurement speed. Although the imaging speed in spontaneous Raman microscopy has improved dramatically in the latest couple of decades, a high-resolution imaging mode, *e.g.*, with 1024×1024 image pixels, can still typically take an hour or longer [28].

Here, we present multiline illumination confocal Raman microscopy, where the detection of separate regions of the sample is performed in parallel, enabling spontaneous Raman hyperspectral imaging as fast as ~10 min/megapixels. This new technique uses multiple line illuminations for scanning a sample and consequently accelerates spontaneous Raman microscopic imaging in comparison to a conventional slit-scanning Raman microscopy using a single slit by a factor of N, where N is the number of illumination lines (See Fig. S1 and the relevant explanations in Supplement 1). By using the developed technique, we demonstrated fast Raman imaging of large tissue samples as well as living cells. The improvement of the image acquisition time demonstrated in this research expands the possible applications of Raman microscopy in biological and medical fields.

2. Development of a multiline illumination confocal Raman microscope

The fundamental idea in implementing a multiline illumination Raman microscope is to expand the conventional slit-scanning Raman microscopy, where a line-shaped laser beam illuminates a sample, and the illuminated region is projected to the entrance slit of a spectrophotometer. In the multiline-illumination modality, the spectrophotometer is equipped with a slit array and the sample is illuminated with multiple line-shaped laser foci. When scattering light from the illuminated regions is projected onto the multiple slits at the spectrophotometer entrance, a comb-like Raman hyperspectral image with spatial information of the irradiated regions is captured. By scanning the sample with multiline illumination, a two-dimensional Raman hyperspectral image is acquired.

There are three essential and unique points in the optical design for multiline illumination Raman microscopes; one is the determination of the distance between adjacent slits in the slit array, D. Because the horizontal axis of the spectrophotometer detector is used not only for recording spectra but also for acquiring the spatial information of the sample, D determines, together with the spectrophotometer dispersion, the spectral range measurable without overlapping of spectra from the other slits on the detector. Another point in the design is the determination of a distance between the two furthest slits at the slit array, W. Spacing of these two slit images at the spectrophotometer detector needs to be smaller than or equivalent to $L - D \times M$, where L is the length of the detector in the spectrophotometer dispersion axis and M is the spectrophotometer magnification. Furthermore, the optical properties of the spectrophotometer such as off-axis

aberrations and F-number can practically limit W that remains useful for Raman spectral imaging without significant aberration and vignetting. Apparently, the maximum number of slits is then $(W + D)/D$. The last point in the design is the degree of difficulty in matching between the illumination pattern and the slit array.

With consideration of the above points, we developed a multiline illumination confocal Raman microscope. Figure 1 depicts a schematic view of the multiline illumination Raman microscope. A single-frequency continuous laser at $\lambda = 532$ nm (Millennia-eV 25W, Spectra Physics) was used. The laser beam was expanded by a beam expander and was formed into multiple line-shaped beams by a cylindrical lens array (Edmund Optics). The space between two adjacent illumination lines was set to 600 µm by a beam expander, which corresponds to the separation of the two adjacent slits. The multiple line-shaped beams were relayed and focused onto the sample plane through a microscope objective lens (CFI Plan Apochromat Lambda 60XC or CFI75 Apochromat 25XC, Nikon). Raman scattering from the sample irradiated by the multiline illumination was collected by the same objective lens and guided to the lens-based spectrophotometer (CLP-300, Bunkoukeiki) equipped with a water-cooled CCD camera having 13.5 µm × 13.5 µm pixels (PIXIS 2048B, Teledyne Instruments) and a reflection grating having 150 g/mm groove density and 500 nm blaze wavelength. At the entrance of the spectrophotometer, a custom confocal slit array made by vapor deposition of metal on a quartz window with a patterning mask was placed. The slit period was 600 µm so that each spectrum was measured by ~44 pixels of the detector, with a spectral range and pixel resolution of $330-400$ cm^{-1} and $8-10$ cm^{-1}, respectively, depending on the detected wavenumber region. The slit width was determined by the point spread function of the detection optics. We set the slit width to 30 µm for the 25× objective lens (equivalent to $1.4-1.5$ Airy units) and 60 µm for the 60× objective lens (~1.0 Airy units). A galvanometer mirror was used to scan the sample with the laser beams. To avoid excess sample irradiation by the laser beams, we put a mechanical shutter in the excitation path and opened it only when the spectrophotometer camera was exposed for data acquisition.
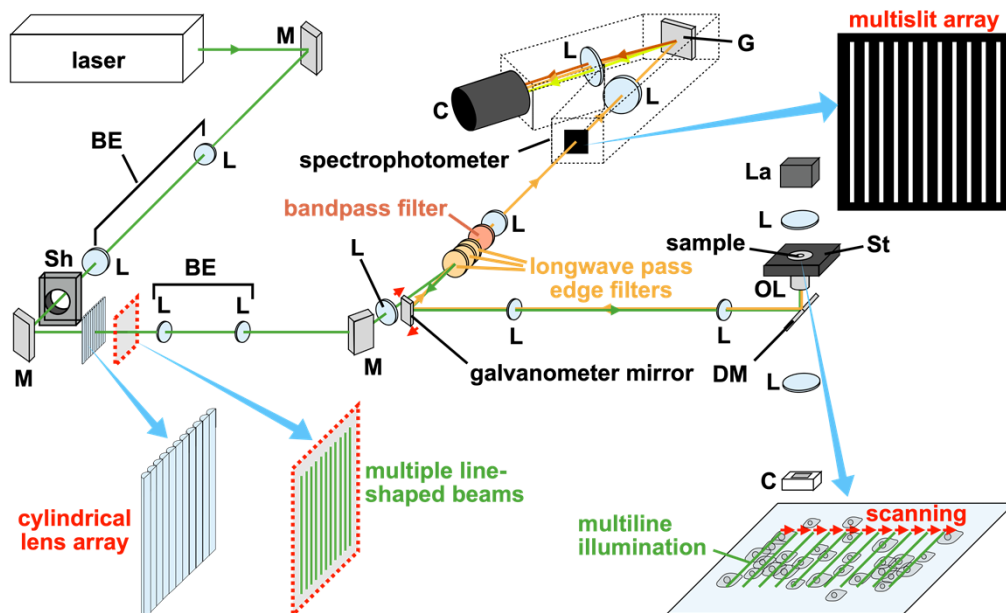

Fig. 1. A schematic diagram of a custom-built multiline illumination confocal Raman microscope. M: mirror. L: lens. BE: beam expander. Sh: shutter. DM: dichroic mirror. OL: objective lens. St: stage. La: Lamp (halogen). C: camera. G: grating.

To avoid spectral overlapping at the detector between adjacent irradiated regions, we limited the spectral range of the Raman scattering entering the spectrophotometer by placing a bandpass filter in the detection path between an edge filter and the imaging lens located in front of the spectrophotometer entrance. Selection of the bandpass filter was based on the appropriate passband values, steepness of the cutoff, and high transmittance. The passband was also tuned to the spectral range of interest by adjustment of the angle of incidence. We also installed additional longwave pass edge filters at the detection path. Hence, we avoided overlaps of laser excitation and Rayleigh scattering light on the Raman spectra as well as eliminating spectral overlap of different measurement regions on the CCD camera.

Choices of detailed experimental conditions and parameters, including objective lens, grating, slit array, bandpass filter, and camera settings, depended on the measurement applications demonstrated here. Such detailed conditions and parameters for the different individual measurements are described in the following sections. Guidance for selecting camera readout conditions is provided in Supplement 1.

3. Results

3.1. Polymer beads measurement as a proof-of-concept experiment

To ensure that a hyperspectral Raman image is taken by the constructed multiline illumination Raman microscope, we first used polymer beads as a sample because its size, shape, spectra, and spatial distribution can be validated by other means. We suspended polystyrene (PS) beads of diameters of 1 μm (Polysciences) and polymethyl methacrylate (PMMA) beads of diameters of 0.8 μm (Soken Chemical & Engineering) in deionized distilled water. They were cast and dried on MAS-coated coverslip (No. 1S, Matsunami Glass).

The mixture of polymer beads was irradiated with 21 line-shaped beams having a constant spacing between adjacent two lines (Fig. 2(A)). With a frame acquisition by the spectrophotometer camera, a comb-like Raman hyperspectral image having the spatial information at the irradiated regions was acquired (Fig. 2(B)). The signal accumulation time for each frame acquisition was 5 s. The CCD readout rate was 100 kHz. By stepwise scanning with frame acquisitions, a series of comb-like hyperspectral image data was acquired. We chose the sampling condition of ~0.21 μm/pixel in the scanning axis to measure small beads with a high spatial resolution. The acquired data was then converted to a three-dimensional data cube, consisting of 798×800 image pixels ($x \times y$) and 43 spectral pixels. Representative Raman spectra are shown in Fig. 2(C). The spectra show characteristic bands at $3051\,\mathrm{cm}^{-1}$ and $2953\,\mathrm{cm}^{-1}$ of PS and PMMA, respectively [20].

From the dataset, Raman images were reconstructed (see Supplement 1 for "Raman image reconstruction process and postprocess"). By the intensity at $3051\,\mathrm{cm}^{-1}$ and $2953\,\mathrm{cm}^{-1}$, the Raman images representing the spatial distributions of PS and PMMA beads were reconstructed (Fig. 2(D)). Figure 2(E) shows the magnified views of regions near the center and the corner. The signal-to-noise ratio (SNR) in the corner is lower than the center, possibly due to the excitation intensity inhomogeneity resulting from the gaussian profile of the excitation laser. Because of the low SNR, the practical spatial resolution can be degraded.

The hyperspectral Raman image data consists of $903 \times 800 \times 38$ pixels in its original form, where 903×800 is the number of the spectrophotometer camera pixels used for each frame acquisition and 38 is the number of scanning steps. As each frame requires the acquisition time of 12.2 s including 5.0 s camera exposure and 7.2 s camera readout, the total image acquisition time was 7.7 min (12.2 s/frame $\times$ 38 frames). In comparison, the conventional line illumination technique using a single line-shaped beam requires 798 (= 38×21) scanning steps, resulting in a 21-fold image acquisition time (= 162 min) for measuring the same sample region under the same laser intensity and frame pixel number.
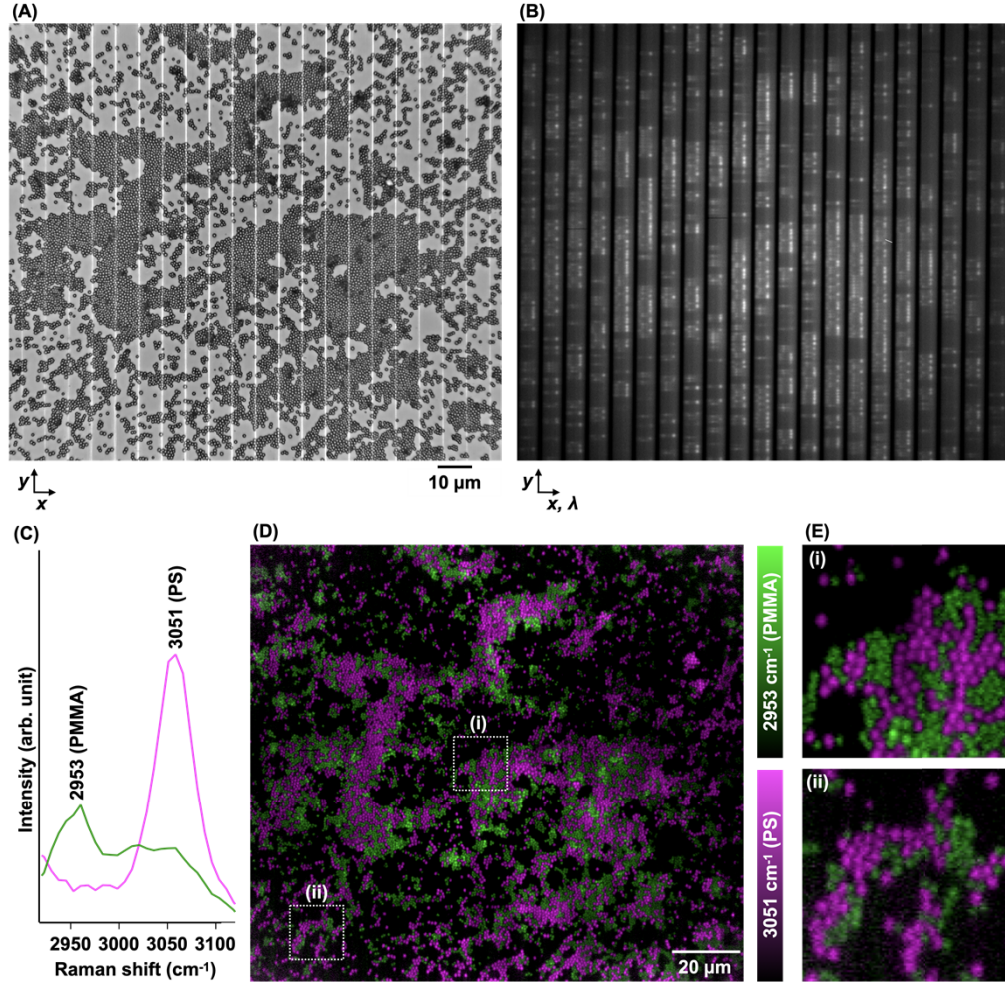
Fig. 2. Raman hyperspectral imaging of a mixture of PS and PMMA beads by the constructed multiline illumination Raman microscope. (A) Bright-field image of the sample irradiated with 21 illumination lines. (B) An image frame acquired by the spectrophotometer camera with the sample shown in (A). (C) Representative Raman spectra from the regions indicated by arrows in B. (D) Raman images reconstructed by the intensity at $3051\,\mathrm{cm^{-1}}$ (magenta) and $2953\,\mathrm{cm^{-1}}$ (green) presenting spatial distributions of PS and PMMA beads, respectively. The image consists of 798×800 pixels. (E) The magnified views of the bead images near the center (i) and a corner (ii) of the field of view in (D). We used the 60× objective lens, the multislit in 60 µm width, and a bandpass filter allowing the selective detection of 2920–$3120\,\mathrm{cm^{-1}}$. We used ethanol Raman bands for wavenumber calibration of the spectrophotometer.

3.2. Mouse tissue measurement

We applied the new modality to measure mouse tissue and determine the capabilities for biomedical tissue imaging applications. Kidney and liver tissue samples were handled with the approval of and in accordance with guidelines from the Animal Research Committee of Kyoto Prefectural University of Medicine (Approval No. M2019-200). Brain tissue samples were handled with the approval by the Animal Care and Use Committee of Osaka University (Approval No. Douyaku 28-1). All efforts were made to minimize the number of animals used. Adult male mice (C57BL/6J) were anesthetized with a mixture containing medetomidine (Nippon Zenyaku Kogyo), midazolam (Astellas Pharma or Sandoz Pharma), and butorphanol (Meiji Seika Pharma) and perfused with 4% paraformaldehyde solution in phosphate-buffered saline (PBS). The kidney, liver, and brain were resected from the mice and immersed in 4% paraformaldehyde in PBS solution overnight. The tissue was sliced with a cryotome (CM1900 or CM1520, Leica Microsystems) into sections with either a 10 μm or 50 μm thickness. Each section was placed on a glass coverslip and immersed in PBS.

Figure 3 shows the results of tissue imaging using 21 simultaneous illumination lines. In the kidney results, the acquired spectra exhibit characteristic Raman bands at 1578 and 2930 cm^{-1} (Fig. 3(A)). The 2930 cm^{-1} band can be assigned to CH$_3$ stretching vibrations of proteins [29], while the 1578 cm^{-1} band can be attributed to ferrous cytochromes *b* and *c* at resonant excitation by 532 nm light [10,30]. The kidney Raman image reconstructed by these bands is shown in Fig. 3(B). The protein distribution represents the complex glomerulus structures (*i.e.*, capillary vessels, supporting cells, and extracellular materials) and the renal tubules (*e.g.*, collecting tubules, proximal tubules, and distal tubules). The cytochrome distribution exhibits less content of the reduced cytochromes in the glomeruli than in the tubules, consistent with an immunohistochemical study of cytochrome protein expression [31] and possibly reflecting the active ion transport by mitochondria in tubules and the passive filtration process in glomeruli [32]. The cytochrome distribution was also varied among the tubules. This variation can be associated with the redox states of cytochrome *c* predominantly existing in mitochondria because it was reported that the redox state of mitochondria differs among renal tubules [33]. In the liver result, acquired spectra exhibit characteristic Raman bands at 1582 and 2930 cm^{-1} as well as a shoulder at 2854 cm^{-1} (Fig. 3(C)). The liver Raman image reconstructed by these bands is shown in Fig. 3(D). The intensity at 2930 cm^{-1}, possibly assigned to a CH$_3$ symmetric stretching mode by proteins and lipids [34,35], visualizes the liver histology with hepatic cords. The intensities at 2854 and 1582 cm^{-1} can be assigned to lipid and retinol, respectively [35,36]. Lipid and retinol contents in the liver can reflect the state of non-alcoholic fatty liver disease [35,36]. In the brain results, acquired spectra exhibit a characteristic Raman band at 2930 cm^{-1} assigned to a CH$_3$ symmetric stretching mode [37] and a shoulder at 2854 cm^{-1} representing lipid content [20] (Fig. 3(E)). The brain Raman image reconstructed by the intensities at 2854 and 2930 cm^{-1} are shown in Fig. 3(F). The image exhibits the distinctive layer with less lipid content. This lipid-poor layer corresponds to the granular cell layer of the hippocampal dentate gyrus, that is densely populated with cell bodies. The lipid-rich regions correspond to the polymorphic cell layer (at center and center-right) and the molecular layer (at top-left and bottom-center), which are rich in dendrites and axons. The myelin sheath necessary for saltatory conduction in dendrites and axons is rich in lipid.

We chose the sampling conditions of ~0.86 μm/pixel in *x* direction to measure global tissue structures with a short acquisition time as well as a relatively low resolution, and consequently the image size was 462 × 800 pixels for liver and kidney. Three continuing regions were measured for brain imaging and initially had 1386 (= 462 × 3) pixels in *x* direction but the overlapping regions were removed so that the resultant final image size in *x* was 1351 pixels.

For each hyperspectral image reconstructed by 22 frames of 903 × 800 pixels each, the total data acquisition time was 3.8 min, since the acquisition time of each frame required 10.36 s
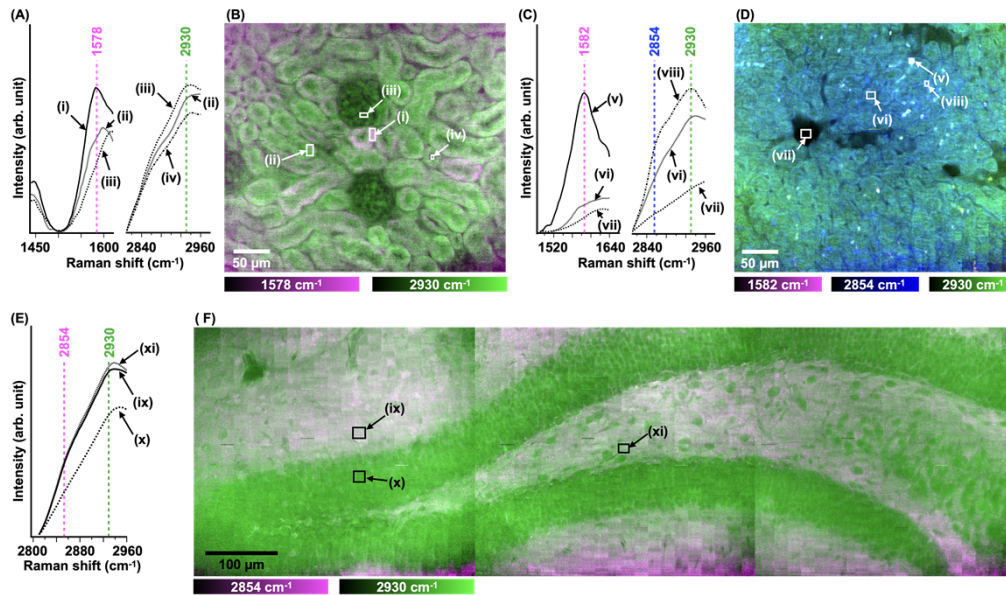
Fig. 3. Mouse tissue spectra (A,C,E) and images (B,D,F) acquired from kidney (A,B), liver (C,D), and brain (E,F) with multiline illumination Raman microscopy. The kidney and liver images consist of 462×800 pixels. The brain image consists of 1351×800 pixels. The spectra were taken from the regions indicated in the images. Each spectrum was normalized by the minimal intensity in the range so that the difference between spectra can be clearly seen. The regions indicated by Roman numerals can be (i,ii) renal tubules, (iii) glomerulus, (iv) lumen of renal tubule, (v) hepatic stellate cell, (vi) nucleus of hepatocyte, (vii) lumen of central vein, (viii) cytoplasm of hepatocyte, (ix) molecular layer, (x) granular cell layer, and (xi) polymorphic cell layer. We used the 25× lens, the slit array of 30 µm width, and a bandpass filter allowing the selective detection of 2810–2960, 1440–1620, or 1490–1640 cm^{-1}. The laser intensity at the sample was estimated to be 1 mW/µm^2. We used ethanol Raman bands for wavenumber calibration of the spectrophotometer.

including 10.00 s camera exposure and 0.36 s camera readout (at 2 MHz). For the observations of kidney and liver tissues, we sequentially acquired two images with a total imaging time of 7.6 min. For the brain imaging, it took 11.4 min for acquiring 66 frames of 903×800 pixels each. Since the number of illumination lines was 21, the number of spectra sampled was 1108800 (= $800 \times 66 \times 21$). Converting this high-throughput sampling to an effective single pixel dwell time gives 617 µs.

3.3. Live-cell measurement

We also measured living cells for further demonstrating the utility of multiline Raman imaging in biomedical single applications. HeLa cells were seeded on calcium fluoride substrate (0.2 mm thickness, Crystran) with a cell density of 1×10^5 cells, and cultured in an incubator (37 °C and 5% CO$_2$ environment) for 48 h. Dulbecco's Modified Eagle's Medium (DMEM: Wako) with 10% fetal bovine serum and 1% penicillin-streptomycin-glutamine was used as a cellular growing medium.

Figure 4(A) shows the representative Raman spectra at 2800–3000 cm^{-1}. The band at 2930 cm^{-1} is assigned to the CH$_3$ symmetric stretching mode [1], representing protein contents in living cells [38], while the band at 2854 cm^{-1} is assigned to CH$_2$ symmetric stretching mode and represents lipid content in living cells [1]. By using the intensity of these representative

bands, a Raman image was reconstructed as shown in Fig. 4(B). Lipid droplets are identified by the lipid signal mostly at the periphery of nuclei and nucleoli are identified by the protein signal in the nuclei. Those molecular distributions are consistent with the types of results obtained by the single-line illumination technique [10,38].
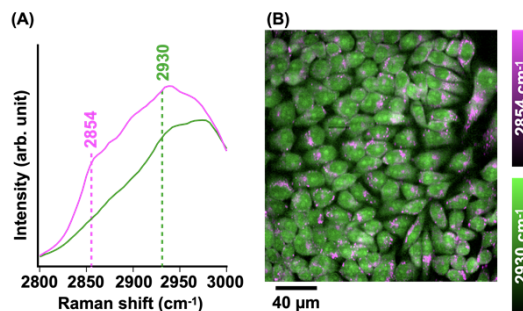

Fig. 4. Live-cell imaging by multiline illumination Raman microscopy. (A) Representative Raman spectra in the ranges of 2800–3000 cm^{-1}. (B) The Raman image reconstructed with the intensity of 2854 cm^{-1} (magenta), and 2930 cm^{-1} (green). The image consists of 462 × 512 pixels. We used the 25× objective lens, the slit array of 30 µm width, and a bandpass filter allowing the selective detection of 2800–3000 cm^{-1}. The signal accumulation time for each frame acquisition was 10 s. The CCD readout rate was 100 kHz. The total image acquisition time was 8.7 min. The laser intensity at the sample was estimated to be 3 mW/µm². We used ethanol Raman bands for wavenumber calibration of the spectrophotometer.

The number of line-shaped laser beams was reduced from 21 to 11 for live-cell imaging. The reduction of the number of beams lowered the background contributions, mainly from water. This is because the buffer solution of the cell sample at the out of focus contributed to the spectral background and this background becomes larger when more line-illumination beams are used under the same irradiation dose for each line-illumination beam. The line length was reduced to lower the spectral background for the same reason. The length reduction resulted in the pixel number reduction in *y* from 800 to 512.

4. Discussions

Multiline illumination confocal Raman microscopy accelerated Raman hyperspectral imaging by parallel detection using a line illumination array, where the image acquisition time can be improved with the number of illumination lines used for imaging. In our demonstration, the polymer bead sample was measured using 21 illumination lines, and a corresponding 21-fold improvement of image acquisition time was then confirmed, in comparison to the conventional single-line illumination technique. In the observation of the mouse tissue, we demonstrated fast Raman hyperspectral imaging, sampling 1108800 spectra in 11.4 min. Converting this high-throughput sampling to an effective single pixel dwell time gives 617 µs. This value is still slower than the typical pixel dwell time in fluorescence confocal laser scanning microscopy, but is comparable with some fluorescence modalities, *e.g.*, by super-resolution fluorescence microscopy [39,40].

In comparison to the conventional confocal or slit-scanning Raman microscopes, multiline illumination Raman microscopy as implemented here has a limitation in the detectable spectral region with one exposure. For complex spectral analysis, this can be an issue. However, Raman imaging does not always require a wide spectrum range. Cell and tissue classifications, such as for cancer diagnosis, can be performed using only limited bands in a Raman spectrum [28,41–45]. Many works for biomedical applications have also been demonstrated by using

only the high wavenumber region especially in CARS/SRS microscopy [2, 46–49]. Vibrational tags, recently emerging labeling technologies enabling small-molecule imaging of biological samples [1,16,23–27], are also well-suited for multiline illumination Raman microscopy, because characteristic bands of the tags have bandwidths as narrow as 13 cm^{-1} full width at half maximum [26]. In addition, the presented technique also allows users to adjust the actual microscope for their needs and samples, based on the unique tunability in spectral range and throughput (in terms of image area per time or samples per time). One limitation on the tunability lies on measurement focusing in small samples, such as a single cell, whose size is in the range of 10−50 µm in many cases. In the presented result, the distance between adjacent two slits was 600 µm, corresponding to a detectable spectral range of 330–400 cm^{-1} and the illumination line spacing of 8 µm (for the 60× objective) or 19.2 µm (for the 25× objective) at the sample plane. It is not effective to increase the detectable spectral range in these cases because the benefit in imaging speed of multiline illumination Raman microscopy will become diminished.

Since the number of camera pixels has been increasing in recent technology development, it is timely to consider how multiline-scanning or multiplex techniques can offer more flexibility in spontaneous Raman microscopy and spectroscopy. We now have the option to design hyperspectral imaging that makes the most efficient use of image sensor pixels and allows us to tune the range of spectrum detection for maximizing the investigation speed. This leads us also to consider what the limitations are, since one could imagine scaling up the multiplexed detection to higher levels. One main limitation of the technique presented here is the requirement for relatively high laser irradiation dose, and the associated increases in background spectral level due to scattering and luminescence coming from out-of-focus planes or possible damage of the optical elements, such as the lenses. Any temperature rise in the sample would also cause acceleration of sample damage, although as the results here show, it is possible to keep the excitation intensity at a similar level to confocal or slit-scanning Raman microscopy, and achieve many-fold improvement in imaging speed.

Multiline illumination Raman microscopy can further accelerate the measurement in several ways, first, by use of a fast camera with low-level noise. The cooled CCD camera used here has relatively high readout noise [28] and slow readout speed. The high readout noise tends to increase measurement time because long signal accumulation time can be generally required in a measurement with a high noise. Besides this, an increment of the number of spectra that are taken by a single camera frame acquisition can also accelerate the measurement by multiline illumination Raman microscopy. In this work, 16800 spectra were taken at maximum with 21 line illuminations and 903×800 detector pixels. Because we used a camera having 2048×2048 pixels, the number of spectra taken by the single line illumination can be increased up to 2048 while the number of line illuminations can be increased up to 47 (*i.e.*, $21 \times 2048 / 903$). Indeed, the imaging system we developed cannot simply support further increment in the spectra number increment primarily because it has a limited effective field number of ~13. Optimizing the system for a larger field of view corresponding to the objective lens field number, i.e., 22 for the 25×/1.1 NA water immersion objective lens, could lead to further improvement. Some applications will also benefit from combination with other high-speed Raman measurement approaches using, *e.g.*, selective sampling [50], compressed sensing [17,51], surface-enhanced Raman scattering [15,16,52], machine learning [53], and coherent Raman scattering [54], for further acceleration of the measurement.

The capability to acquire images at high speed and to adjust the detection wavenumber range removes one of the major limitations of vibrational imaging in life sciences. With the advent of small molecule imaging, metabolic imaging, and multiplex imaging using vibrational tags, we will be able to obtain biological information that is not available with conventional fluorescence techniques. In order to take advantage of these technologies, it is important to shorten the image acquisition time, and the multiline illumination scan technology can play a significant role.

Sensitivity is also an issue in Raman imaging, and the multiline illumination scan technology can address this as well, since it can acquire more signals in the same exposure time compared to the conventional single focus or slit scanning techniques. Besides the above, other practical applications of Raman microscopy in medicine can be boosted by multiline illumination confocal Raman microscopy. One of the major reasons that Raman microscopy has not been adopted in hospitals is the inherent slow speed. However, many studies have shown the usefulness of Raman microscopy for label-free detection of cancer cells and tissue [28,55,56], peripheral nerves [44,57], myocardial infarction [58,59], and fatty liver [34–36,60]. Thus, multiline illumination confocal Raman microscopy has a potential to assist medical diagnosis and care through label-free, high-speed hyperspectral imaging using molecular fingerprints.

Supplemental document. See Supplement 1 for supporting content.

References

1. A. F. Palonpon, J. Ando, H. Yamakoshi, K. Dodo, M. Sodeoka, S. Kawata, and K. Fujita, "Raman and SERS microscopy for molecular imaging of live cells," Nat. Protoc. **8**(4), 677–692 (2013).
2. F. Hu, L. Shi, and W. Min, "Biological imaging of chemical bonds by stimulated Raman scattering microscopy," Nat. Methods **16**(9), 830–842 (2019).
3. B. Durrant, M. Trappett, D. Shipp, and I. Notingher, "Recent developments in spontaneous Raman imaging of living biological cells," Curr. Opin. Chem. Biol. **51**, 138–145 (2019).
4. W. Chen, G. A. Lemieux, C. H. Camp Jr, T. Chang, K. Ashrafi, and M. T. Cicerone, "Spectroscopic coherent Raman imaging of Caenorhabditis elegans reveals lipid particle diversity," Nat. Chem. Biol. **16**(10), 1087–1095 (2020).
5. K. Kong, C. Kendall, N. Stone, and I. Notingher, "Raman spectroscopy for medical diagnostics — From in-vitro biofluid assays to in-vivo cancer detection," Adv. Drug Delivery Rev. **89**, 121–134 (2015).
6. K. J. I. Ember, M. A. Hoeve, S. L. McAughtrie, M. S. Bergholt, B. J. Dwyer, M. M. Stevens, K. Faulds, S. J. Forbes, and C. J. Campbell, "Raman spectroscopy and regenerative medicine: a review," NPJ Regener. Med. **2**(1), 12 (2017).
7. A. Zumbusch, G. R. Holtom, and X. S. Xie, "Three-dimensional vibrational imaging by coherent anti-Stokes Raman scattering," Phys. Rev. Lett. **82**(20), 4142–4145 (1999).
8. C. L. Evans, E. O. Potma, M. Puoris'haag, D. Côté, C. P. Lin, and X. S. Xie, "Chemical imaging of tissue in vivo with video-rate coherent anti-Stokes Raman scattering microscopy," Proc. Natl. Acad. Sci. U. S. A. **102**(46), 16807–16812 (2005).
9. C. H. Camp Jr, Y. J. Lee, J. M. Heddleston, C. M. Hartshorn, A. R. H. Walker, J. N. Rich, J. D. Lathia, and M. T. Cicerone, "High-speed coherent Raman fingerprint imaging of biological tissues," Nat. Photonics **8**(8), 627–634 (2014).
10. K. Hamada, K. Fujita, N. I. Smith, M. Kobayashi, Y. Inouye, and S. Kawata, "Raman microscopy for dynamic molecular imaging of living cells," J. Biomed. Opt. **13**(04), 1 (2008).
11. M. Okuno and H. Hamaguchi, "Multifocus confocal Raman microspectroscopy for fast multimode vibrational imaging of living cells," Opt. Lett. **35**(24), 4096–4098 (2010).
12. C. W. Freudiger, W. Min, B. G. Saar, S. Lu, G. R. Holtom, C. He, J. C. Tsai, J. X. Kang, and X. S. Xie, "Label-free biomedical imaging with high sensitivity by stimulated Raman scattering microscopy," Science **322**(5909), 1857–1861 (2008).
13. B. G. Saar, C. W. Freudiger, J. Reichman, C. M. Stanley, G. R. Holtom, and X. S. Xie, "Video-rate molecular imaging in vivo with stimulated Raman scattering," Science **330**(6009), 1368–1370 (2010).
14. Y. Ozeki, W. Umemura, Y. Otsuka, S. Satoh, H. Hashimoto, K. Sumimura, N. Nishizawa, K. Fukui, and K. Itoh, "High-speed molecular spectral imaging of tissue with stimulated Raman scattering," Nat. Photonics **6**(12), 845–851 (2012).

15. K. Fujita, S. Ishitobi, K. Hamada, N. I. Smith, A. Taguchi, Y. Inouye, and S. Kawata, "Time-resolved observation of surface-enhanced Raman scattering from gold nanoparticles during transport through a living cell," J. Biomed. Opt. **14**(2), 024038 (2009).

16. K. Koike, K. Bando, J. Ando, H. Yamakoshi, N. Terayama, K. Dodo, N. I. Smith, M. Sodeoka, and K. Fujita, "Quantitative drug dynamics visualized by alkyne-tagged plasmonic-enhanced Raman microscopy," ACS Nano **14**(11), 15032–15041 (2020).

17. N. Pavillon and N. I. Smith, "Compressed sensing laser scanning microscopy," Opt. Express **24**(26), 30038–30052 (2016).

18. F. Soldevila, J. Dong, E. Tajahuerce, S. Gigan, and H. B. De Aguiar, "Fast compressive Raman bio-imaging via matrix completion," Optica **6**(3), 341–346 (2019).

19. S. Ayas, G. Cinar, A. D. Ozkan, Z. Soran, O. Ekiz, D. Kocaay, A. Tomak, P. Toren, Y. Kaya, I. Tunc, H. Zareie, T. Tekinay, A. B. Tekinay, M. O. Guler, and A. Dana, "Label-free nanometer-resolution imaging of biological architectures through surface enhanced Raman scattering," Sci. Rep. **3**(1), 2624 (2013).

20. K. Watanabe, A. F. Palonpon, N. I. Smith, L. Chiu, A. Kasai, H. Hashimoto, S. Kawata, and K. Fujita, "Structured line illumination Raman microscopy," Nat. Commun. **6**(1), 10095 (2015).

21. Y. Yonemaru, A. F. Palonpon, S. Kawano, N. I. Smith, S. Kawata, and K. Fujita, "Super-spatial- and -spectral-resolution in vibrational imaging via saturated coherent anti-Stokes Raman scattering," Phys. Rev. Appl. **4**(1), 014010 (2015).

22. L. Gong, W. Zheng, Y. Ma, and Z. Huang, "Higher-order coherent anti-Stokes Raman scattering microscopy realizes label-free super-resolution vibrational imaging," Nat. Photonics **14**(2), 115–122 (2020).

23. H. Yamakoshi, K. Dodo, M. Okada, J. Ando, A. F. Palonpon, K. Fujita, S. Kawata, and M. Sodeoka, "Imaging of EdU, an alkyne-tagged cell proliferation probe, by Raman microscopy," J. Am. Chem. Soc. **133**(16), 6102–6105 (2011).

24. H. Yamakoshi, K. Dodo, A. Palonpon, J. Ando, K. Fujita, S. Kawata, and M. Sodeoka, "Alkyne-tag Raman imaging for visualization of mobile small molecules in live cells," J. Am. Chem. Soc. **134**(51), 20681–20689 (2012).

25. L. Wei, Z. Chen, L. Shi, R. Long, A. V. Anzalone, L. Zhang, F. Hu, R. Yuste, V. W. Cornish, and W. Min, "Super-multiplex vibrational imaging," Nature **544**(7651), 465–470 (2017).

26. F. Hu, C. Zeng, R. Long, Y. Miao, L. Wei, Q. Xu, and W. Min, "Supermultiplexed optical imaging and barcoding with engineered polyynes," Nat. Methods **15**(3), 194–200 (2018).

27. L. Shi, C. Zheng, Y. Shen, Z. Chen, E. S. Silveira, L. Zhang, M. Wei, C. Liu, C. de Sena-Tomas, K. Targoff, and W. Min, "Optical imaging of metabolic dynamics in animals," Nat. Commun. **9**(1), 2995 (2018).

28. Y. Kumamoto, K. Mochizuki, K. Hashimoto, Y. Harada, H. Tanaka, and K. Fujita, "High-throughput cell imaging and classification by narrowband and low-spectral-resolution Raman microscopy," J. Phys. Chem. B **123**(12), 2654–2661 (2019).

29. Z. Movasaghi, S. Rehman, and I. U. Rehman, "Raman spectroscopy of biological tissues," Appl. Spectrosc. Rev. **42**(5), 493–541 (2007).

30. T. G. Spiro and T. C. Strekas, "Resonance Raman spectra of hemoglobin and cytochrome c: Inverse polarization and vibronic scattering," Proc. Natl. Acad. Sci. U. S. A. **69**(9), 2622–2626 (1972).

31. M. Zhan, I. M. Usman, L. Sun, and Y. S. Kanwar, "Disruption of renal tubular mitochondrial quality control by myo-inositol oxygenase in diabetic kidney disease," J. Am. Soc. Nephrol. **26**(6), 1304–1321 (2015).

32. P. Bhargava and R. G. Schnellmann, "Mitochondrial energetics in the kidney," Nat. Rev. Nephrol. **13**(10), 629–646 (2017).

33. A. M. Hall, R. J. Unwin, N. Parker, and M. R. Duchen, "Multiphoton imaging reveals differences in mitochondrial function between nephron segments," J. Am. Soc. Nephrol. **20**(6), 1293–1302 (2009).

34. T. Minamikawa, M. Ichimura-Shimizu, H. Takanari, Y. Morimoto, R. Shiomi, H. Tanioka, E. Hase, T. Yasui, and K. Tsuneyama, "Molecular imaging analysis of microvesicular and macrovesicular lipid droplets in non-alcoholic fatty liver disease by Raman microscopy," Sci. Rep. **10**(1), 18548 (2020).

35. K. M. Helal, J. N. Taylor, H. Cahyadi, A. Okajima, K. Tabata, Y. Itoh, H. Tanaka, K. Fujita, Y. Harada, and T. Komatsuzaki, "Raman spectroscopic histology using machine learning for nonalcoholic fatty liver disease," FEBS Lett. **593**(18), 2535–2544 (2019).

36. M. Takemura, K. Mochizuki, Y. Harada, A. Okajima, M. Hayakawa, P. Dai, Y. Itoh, and H. Tanaka, "Label-free assessment of the nascent state of rat non-alcoholic fatty liver disease using spontaneous Raman microscopy," Acta Histochem. Cytochem. **55**(2), 22-0001357 (2022).

37. A. Mizuno, T. Hayashi, K. Tashibu, S. Maraishi, K. Kawauchi, and Y. Ozaki, "Near-infrared FT-Raman spectra of the rat brain tissues," Neurosci. Lett. **141**(1), 47–52 (1992).

38. Y. Kumamoto, Y. Harada, T. Takamatsu, and H. Tanaka, "Label-free molecular imaging and analysis by Raman spectroscopy," Acta Histochem. Cytochem. **51**(3), 101–110 (2018).

39. Y. Nawa, Y. Yonemaru, A. Kasai, R. Oketani, H. Hashimoto, N. I. Smith, and K. Fujita, "Saturated excitation microscopy using differential excitation for efficient detection of nonlinear fluorescence signals," APL Photonics **3**(8), 080805 (2018).

40. F. Göttfert, T. Pleiner, V. Westphal, D. Görlich, S. J. Sahl, and S. W. Hell, "Strong signal increase in STED fluorescence microscopy by imaging regions of subdiffraction extent," Proc. Natl. Acad. Sci. U. S. A. **114**(9), 2125–2130 (2017).

41. S. Duraipandian, W. Zheng, J. Ng, J. J. H. Low, A. Ilancheran, and Z. Huang, "In vivo diagnosis of cervical precancer using Raman spectroscopy and genetic algorithm techniques," Analyst **136**(20), 4328–4336 (2011).

42. A. C. S. Talari, C. A. Evans, I. Holen, R. E. Coleman, and I. U. Rehman, "Raman spectroscopic analysis differentiates between breast cancer cell lines," J. Raman Spectrosc. **46**(5), 421–427 (2015).

43. I. W. Schie, C. Krafft, and J. Popp, "Cell classification with low-resolution Raman spectroscopy (LRRS)," J. Biophoton **9**(10), 994–1000 (2016).

44. Y. Kumamoto, Y. Harada, H. Tanaka, and T. Takamatsu, "Rapid and accurate peripheral nerve imaging by multipoint Raman spectroscopy," Sci. Rep. **7**(1), 845 (2017).

45. I. W. Schie, J. Rüger, A. S. Mondol, A. Ramoji, U. Neugebauer, C. Krafft, and J. Popp, "High-throughput screening Raman spectroscopy platform for label-free cellomics," Anal. Chem. **90**(3), 2023–2030 (2018).

46. D. Orringer, B. Pandian, and Y. Niknafs, *et al.*, "Rapid intraoperative histology of unprocessed surgical specimens via fibre-laser-based stimulated Raman scattering microscopy," Nat. Biomed. Eng. **1**(2), 0027 (2017).

47. T. C. Hollon, S. Lewis, B. Pandian, Y. S. Niknafs, M. R. Garrard, H. Garton, C. O. Maher, K. McFadden, M. Snuderl, A. P. Lieberman, K. Muraszko, S. Camelo-Piragua, and D. A. Orringer, "Rapid intraoperative diagnosis of pediatric brain tumors using stimulated Raman histology," Cancer Res. **78**(1), 278–289 (2018).

48. N. Nitta, T. Iino, and A. Isozaki, *et al.*, "Raman image-activated cell sorting," Nat. Commun. **11**(1), 3452 (2020).

49. T. C. Hollon, B. Pandian, and A. R. Adapa, *et al.*, "Near real-time intraoperative brain tumor diagnosis using stimulated Raman histology and deep neural networks," Nat. Med. (N. Y., NY, U. S.) **26**(1), 52–58 (2020).

50. F. Sinjab, K. Kong, G. Gibson, S. Varma, H. Williams, M. Padgett, and I. Notingher, "Tissue diagnosis using power-sharing multifocal Raman micro-spectroscopy and auto-fluorescence imaging," Biomed. Opt. Express **7**(8), 2993–3006 (2016).

51. C. Scotté, S. Sivankutty, R. A. Bartels, and H. Rigneault, "Line-scan compressive Raman imaging with spatiospectral encoding," Opt. Lett. **45**(19), 5567–5570 (2020).

52. Z. Zhang, K. Bando, K. Mochizuki, A. Taguchi, K. Fujita, and S. Kawata, "Quantitative Evaluation of Surface-Enhanced Raman Scattering Nanoparticles for Intracellular pH Sensing at a Single Particle Level," Anal. Chem. **91**(5), 3254–3262 (2019).

53. H. He, M. Xu, C. Zong, P. Zheng, L. Luo, L. Wang, and B. Ren, "Speeding up the line-scan Raman imaging of living cells by deep convolutional neural network," Anal. Chem. **91**(11), 7070–7077 (2019).

54. S. Kizawa and M. Hashimoto, "Ultrahigh-speed multiplex coherent anti-Stokes Raman scattering microspectroscopy using scanning elliptical focal spot," J. Chem. Phys. **155**(14), 144201 (2021).

55. K. Kong, C. J. Rowlands, S. Varma, W. Perkins, I. H. Leach, A. A. Koloydenko, H. C. Williams, and I. Notingher, "Diagnosis of tumors during tissue-conserving surgery with integrated autofluorescence and Raman scattering microscopy," Proc. Natl. Acad. Sci. U. S. A. **110**(38), 15189–15194 (2013).

56. J. N. Taylor, K. Mochizuki, K. Hashimoto, Y. Kumamoto, Y. Harada, K. Fujita, and T. Komatsuzaki, "High-resolution Raman microscopic detection of follicular thyroid cancer cells with unsupervised machine learning," J. Phys. Chem. B **123**(20), 4358–4372 (2019).

57. M. Minamikawa, Y. Harada, N. Koizumi, K. Okihara, K. Kamoi, A. Yanagisawa, and T. Takamatsu, "Label-free detection of peripheral nerve tissues against adjacent tissues by spontaneous Raman microspectroscopy," Histochem. Cell Biol. **139**(1), 181–193 (2013).

58. N. Nishiki-Muranishi, Y. Harada, T. Minamikawa, Y. Yamaoka, P. Dai, H. Yaku, and T. Takamatsu, "Label-free evaluation of myocardial infarction and its repair by spontaneous Raman spectroscopy," Anal. Chem. **86**(14), 6903–6910 (2014).

59. T. Yamamoto, T. Minamikawa, Y. Harada, Y. Yamaoka, H. Tanaka, H. Yaku, and T. Takamatsu, "Label-free evaluation of myocardial infarct in surgically excised ventricular myocardium by Raman spectroscopy," Sci. Rep. **8**(1), 14671 (2018).

60. K. Kochan, E. Maslak, C. Krafft, R. Kostogrys, S. Chlopicki, and M. Baranska, "Raman spectroscopy analysis of lipid droplets content, distribution and saturation level in non-alcoholic fatty liver disease in mice," J. Biophoton **8**(7), 597–609 (2015).